Ukrainian Journal of Physical Optics
ISSUE 4
2026

INTELLIGENT SOYBEAN SEED FRACTION SEGMENTATION SYSTEM BASED ON THE INTEGRATION OF SPECTRAL SIGNATURES AND PRECISION NEURAL NETWORK ARCHITECTURES

S. STEPANENKO*, A. KUZMYCH

Institute of Mechanics and Automatics of Agroindustrial Production of the National Academy of Agrarian Sciences of Ukraine, Department of Mechanical and Technological Problems of Harvesting and Post-Harvest Processing of Grain and Oilseed Crops, 11/1 Vokzalna St, Glevakha, Fastiv district, Kyiv region, 08631, Ukraine
*Corresponding author: stepanenko_s@ukr.net

Received: 15.05.2026

Abstract. This study presents an intelligent quality control system for soybean seeds that integrates multi-channel spectral analysis with YOLOv11n-seg for instance segmentation. A spectral contrast window at 610–680 nm was identified for optimal impurity separation, alongside a 15–20% increase in the absolute reflectance coefficient in the 450 nm and 500 nm spectral channels for damaged seeds. To enhance micro-defect detection, a hybrid dataset that simulated dynamic blur was used. Increasing input resolution to 1280 pixels significantly improved the mAP50-95 to 0.872, representing a 10.1% enhancement for broken grain identification compared to standard 640-pixel models. Hardware implementation on an NVIDIA Jetson AGX Orin achieved a real-time processing rate of 17 FPS with an overall mAP50 of 0.956. These findings establish a physical and algorithmic foundation for high-precision automated seed sorting in smart agriculture applications.

Keywords: diffuse reflectance spectroscopy, multispectral imaging, edge AI processing, optical sorting, reflectance coefficients, spectral signature
UDC: 535.36/.37:681.785:004.932:635.655
DOI: 10.3116/16091833/Ukr.J.Phys.Opt.2026.04016

1. Introduction

The modern grain industry requires highly accurate monitoring of process parameters, the most critical of which are grain loss, grain quality, and flow characteristics. Increasing demands for energy efficiency and process automation (particularly in drying and transportation) necessitate the development of intelligent sensor systems.

Traditional control methods based on selective measurements are gradually being replaced by continuous sensor systems. Of particular importance are piezoelectric sensors (impact systems), ultrasonic sensors, and computer vision-based optical systems [1]. These sensors determine indirect losses by measuring grain flow parameters. In particular, they can determine the actual difference between the input and current flow, thereby identifying technological grain losses in the processing line.

Flow sensors can be classified by operating principle into force-based sensors, which generate a signal based on the dynamic movement or weight of the grains, and volumetric sensors, which determine grain characteristics through interaction with visible (optical), infrared (IR), microwave (RF), ultrasound (ultrasonic), or immersion in the grain bed (paddle). Force sensors have an error of no more than 5%, while volumetric sensors have an error of no more than 3% [2].

Sensory methods operate based on the impact of grains against the sensor surface. For sensory methods, piezoelectric (PVDF) sensors and strain gauges are used, with their signals depending on the flow rate. However, when using PVDF sensors, the measurement error is 3–4% [3]. In piezoelectric sensors, when a grain strikes the sensor, the piezoelectric plate deforms, generating an electrical signal proportional to the impact force.

Ultrasonic sensors operate on the principle of measuring the transit time of ultrasonic waves through a material or the amplitude of the signal. These sensors can measure the flow velocity of a grain stream, its structure and density, and its moisture content. Key parameters of these sensors include the distance between them, the installation angle, and the ultrasonic frequency [1, 4]. Ultrasonic sensors provide an average value and require calibration [5].

Magnetoelastic sensors convert the impact of a grain into a change in the magnetic field. They have high stability, but the sensor data error is about 6% [6]. Nuclear magnetic resonance sensors operate on the interaction between electromagnetic waves and atomic nuclei in an external magnetic field. This enables analysis of sample chemical composition, ensuring high accuracy and sensitivity [1, 7]. As a rule, nuclear magnetic resonance-based sensors are used to determine molecular structure and the content of proteins, fats, and other substances in grain. This makes it possible to determine the molecular structures and composition of the grain.

Infrared (IR) sensors and analyzers operate on the basis of spectroscopy in the near-infrared (NIR) and mid-infrared ranges, measuring the absorption and reflection of infrared light by grain [1, 8, 9]. They are used to determine grain moisture content, as well as the content of oil, protein, starch, and fiber, and to detect foreign contaminants.

Microwave sensors operate similarly to IR sensors, but instead of infrared light, they use radio waves with frequencies ranging from 2 to 20 GHz and measure changes in the amplitude and phase of the radio waves as they pass through a layer of grain [10]. Microwaves penetrate paper, plastic, and cardboard, enabling analysis of pre-packaged goods. Microwave sensors can be integrated directly into conveyor lines for in-line inspection with response times in milliseconds. Unlike X-rays, microwave sensors use low power that does not ionize or alter the product's properties. They are used to measure grain moisture content and to detect low-density contaminants (plastic, glass, wood, stones) that are difficult to detect with X-rays or metal detectors. Radio sensors use lower-frequency radio waves to monitor grain levels in silos and the presence or absence of flow. Capacitive sensors are also used for this purpose. In these sensors, the presence of grain between two parallel plates alters their electrical capacitance [11]. Microwave sensors are most widely used in industry.

The most common optical sensors are cameras and video cameras, which analyze grain color, texture, and size. Most often, images of grain captured by cameras and video cameras are analyzed by artificial intelligence systems [5, 12]. They are frequently incorporated into machine vision systems as a fast means of online monitoring.

In modern control systems, sensor data is processed by neural networks and other software tools that are part of intelligent control systems on the production lines of grain elevators, grain processing plants, and food industry enterprises. These intelligent control systems monitor grain moisture content, contamination, atypical impurities, grain temperature, biological activity, pests, mold fungi, and harmful bacteria, and so on. Particular attention is paid to monitoring grain moisture content and contamination [5].

Thus, the integration of sensors with artificial intelligence-based systems is a promising and rapidly developing field.

The information obtained from the sensors about grain flows is processed using discrete element method modeling [13], statistical signal analysis [14], spectral analysis [15], hyperspectral processing [16], and wavelet analysis [17].

However, the main problem remains the influence of external factors (background noise), which significantly reduce measurement accuracy. Since these factors do not directly determine grain-flow characteristics, the main drawbacks of these sensors are reliability and noise compensation. The reliability of these sensors is significantly affected by machine vibrations and grain-flow irregularities. In particular, the operation of piezoelectric sensors is strongly affected by machine vibrations, which cause random impacts of grains; therefore, it is recommended to install them using damping devices, increase the thickness of the piezoelectric plate [2], and use arrays to reduce the influence of background noise [6]. Electrical interference disrupts the operation of microwave, radio, and capacitive sensors. In particular, temperature, humidity, and air movement in seed and grain cleaning lines significantly affect the operation of microwave and radio sensors [18]. Acoustic noise affects the amplitude and propagation speed of ultrasonic vibrations; therefore, signal filtering is required for the stable operation of ultrasonic sensors [4].

Although background noise from machine operation remains the primary source of error, current research focuses not on the sensor design itself, but on advanced signal processing and environmental adaptation. Consequently, this noise can be effectively compensated for using differential measurements, digital filtering, tailored sensor calibration, sensor arrays, and intelligent processing based on machine learning.

However, due to the indirect nature of these flow measurements, conventional piezoelectric and ultrasonic sensors still exhibit an error margin of 2–5%. To overcome these hardware limitations, contemporary research shifts toward hybrid multimodal systems that combine acoustic or ultrasonic sensors with optical cameras, integrated within IoT frameworks [5]. In such configurations, the sensor data and visual streams are fused and processed by an intelligent system to simultaneously compensate for operational noise, detect structural defects, and evaluate flow heterogeneity.

This transition to intelligent hybrid architectures is vital because grain quality is a highly complex, multi-parametric metric determined by moisture content, contamination, atypical or organic impurities, temperature, biological activity, pest infestation, and fungal or bacterial spoilage.

In particular, the system proposed in [5] uses a combination of IoT sensor nodes to monitor bulk grain motion, yet it relies on basic threshold-based filtering, leaving it highly susceptible to operational vibration and unable to identify specific morphological grain defects. Other contemporary studies have successfully deployed deep learning models for grain quality evaluation; for instance, standard vision systems achieve 88–92% accuracy for single-grain classification under static laboratory conditions. However, existing solutions exhibit significant accuracy degradation when processing dynamic, heterogeneous seed flows in real time, primarily because they lack integration of physical spectral signatures to isolate organic impurities (MOG) and subsurface seed coat damage. Consequently, a critical research gap remains in bridging high-speed spatial instance segmentation and multichannel

optical features, limiting the deployment of these technologies in high-throughput industrial separators.

To address these limitations, the aim of this work is to improve the accuracy and reliability of automated fractional analysis of soybean seeds by developing an advanced neural network model for instance segmentation that integrates physical spectral features of objects with optimized spatial resolution of input data, tailored for real-time edge computing implementation.

2. Method

Soybean seeds from the 2025 harvest, along with associated organic impurities typical of the post-harvest grain processing workflow, were selected as the subjects of the experimental studies.

To create a database and conduct spectroscopic measurements, soybean seeds were used and divided into two subgroups based on morphological characteristics.

(1) Normal grain (NG), characterized by a spherical or slightly elongated shape typical of the crop, with a smooth surface. The color of the seed coat is light yellow or pale. This group is the target of segmentation and exhibits the highest reflectance in the visible spectrum due to seed coat pigmentation.

(2) Broken grain (BG), which includes seeds with compromised seed coat integrity, endosperm chips, or deep cracks. In terms of optical characteristics, this group is distinguished by changes in textural features and a slightly different spectral profile in the NIR range due to the exposure of the grain's internal tissues.

The class of organic impurities (MOG – Matter Other than Grain) consists of residues of soybean plant material that end up in the grain bin during combine harvesting. Main composition of the fraction:

- Dry pods. Fragments of woody (lignified) pods that are brown or gray-brown in color with a wrinkled surface.
- Unripe pods. Green-colored elements containing residual chlorophyll. The presence of such objects creates specific spectral "peaks" in the green region (550 nm), which is an important factor for differentiating impurities.
- Stem residues. Fragments of straw and branches.

The morphological heterogeneity of the impurity class (complex shapes, twisting, and varying degrees of moisture and color) makes its identification with standard color segmentation methods unreliable. This necessitates the use of multispectral analysis to identify robust spectral markers that are independent of objects' visual similarity in RGB space.

The spectral characteristics of grain materials in reflection mode were studied using a custom-built laboratory setup, the schematic of which is shown in Fig. 1.

The setup is based on digital multispectral sensors (the AS7262 series for the visible range of 450–650 nm and the AS7263 series for the near-infrared range of 610–860 nm). To automate the measurement process and control the system's hardware components, an Arduino Uno 2 board (Fig. 2a) is used to perform two main functions: controlling the rotating platform's drive and collecting and transmitting data.

The Arduino Uno 2 microcontroller uses a power driver to start, stabilize the rotational speed, and stop the electric motor of the rotating platform 9.

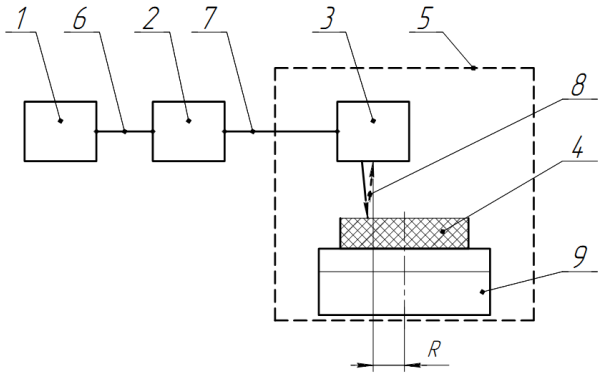

Fig. 1. Schematic diagram of the experimental setup for determining the optical characteristics of grain materials in reflectance mode: 1 – PC; 2 – Arduino Uno board; 3 – digital multispectral sensor; 4 – glass Petri dish with grain material; 5 – lightproof shield; 6 – USB cable; 7 – I2C bus; 8 – near-infrared and visible radiation; 9 – rotating platform.

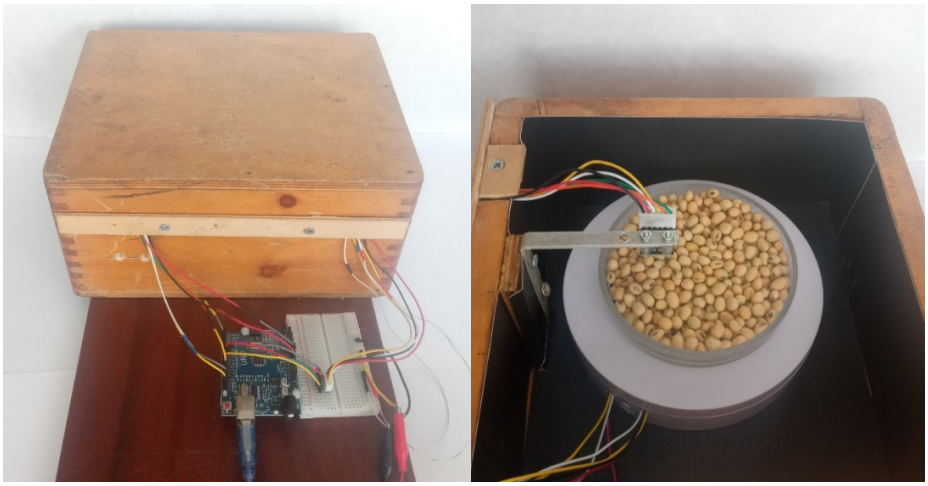

a) b)

Fig. 2. General view of the experimental setup for studying the spectral characteristics of grain materials: a – exterior view showing the light-blocking screen 5, the Arduino Uno 2 connection, and the breadboard; b – interior view with a Petri dish 4 on a rotating platform 9 and a mounted multispectral sensor 3.

Using the I2C digital bus 7, the Arduino board sequentially polls the channels of the multispectral sensor 3, synchronizing the reading times with the dynamic movement of the grain material.

Synchronizing the operation of the drive and sensors has enabled the complete elimination of the human factor during the scanning stage. The read data is transmitted via a USB cable 6 to the serial port of a personal computer (PC) 1. Specialized software written in Python has been developed to read data from the serial port and save it to the hard drive of the PC.

The grain sample under study was placed in a 100-mm-diameter, 20-mm-high glass Petri dish 4. The Petri dish 4 was positioned concentrically on the surface of the cylindrical rotating platform 9 (Fig. 2b). The axis of rotation of the platform 9 is offset relative to the optical axis of the digital multispectral sensor 3 by a distance of R=20 – 25 mm. This allows the sample to be scanned along a circular trajectory to average the readings. The standard LEDs of the sensors served as the radiation source 8. The working distance from the sensor matrix 3 to the surface of the sample layer in the Petri dish was 20 mm.

To eliminate the parasitic influence of external (background) lighting, the measuring chamber was placed inside a light-tight shield 5 (a wooden box), as shown in Fig. 2a.

The study focused on soybean seeds and associated organic impurities. The samples were divided into fractions (Fig. 3): normal grains, broken grains, and MOG. To ensure the statistical significance of the results and account for the stochastic nature of object distribution in the dish, at least 100 discrete measurements were performed for each experiment.

During the spectrometric measurements, it was assumed that the layer of granular material under study was optically infinitely thick. This eliminates distortion of the spectral profiles caused by stray radiation reflected from the setup's structural elements through the gaps between the grains. To physically ensure this condition, a layer of black matte paper (reflectance $\rho < 3\%$) was placed at the bottom of the glass Petri dish before adding the sample. This solution allowed for the complete absorption of radiation passing through the grain bed and ensured that the signal $I_{sample}(\lambda)$ recorded by the sensors was formed exclusively due to single and multiple diffuse reflections from the surface of the objects under study.

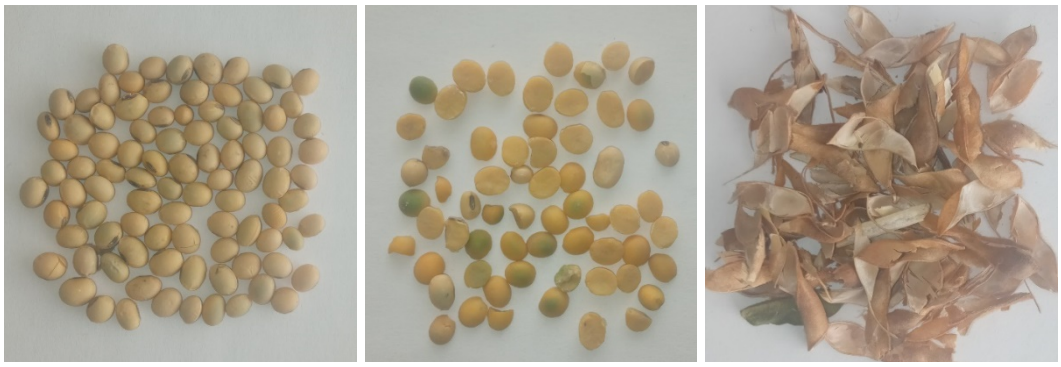

a) b) c)

Fig. 3. Target technological fractions: a) normal grains; b) broken grains; c) organic impurities (MOG).

To minimize the influence of the sensors' hardware characteristics and the non-uniformity of the light source's spectral intensity, the measured intensity values were converted into physical quantities using two-point calibration against white and black working standards. Steel plates with a polymer powder coating (matte finish) were used as working standards. Metrological verification of the comparison standards was performed using a Walcom CM-200S colorimeter (illuminant D65, 45°/0° geometry).

The verified values of the total reflectance (Y) were as follows: white standard – $\rho_{white} = 80.19\%$ (coefficient of variation CV=0.48%); black standard – $\rho_{black} = 2.07\%(\mathrm{CV} = 1.86\%)$.

The absolute spectral reflectance coefficient $R_{abs}(\lambda)$ for each of the 12 channels was calculated using the formula:

$$R_{abs}(\lambda) = \rho_{black} + \frac{I_{sample}(\lambda) - I_{black}(\lambda)}{I_{white}(\lambda) - I_{black}(\lambda)}(\rho_{white} - \rho_{black}), \quad (1)$$

where $I_{sample}(\lambda)$, $I_{white}(\lambda)$, and $I_{black}(\lambda)$ are the intensity values for the test sample, the white standard, and the black standard, respectively.

In the calculations, it was assumed that the working standards were spectrally neutral in the ranges under study (450–650 nm and 610–860 nm). This allowed the spectral reflectance coefficients $\rho_{white}(\lambda)$ and $\rho_{\text{black}}(\lambda)$ to be taken as equal to the integral reflectance coefficients ρ_{white} and ρ_{black}, measured by the colorimeter. The possible spectral deviation of the standards in the NIR region does not exceed the setup's overall measurement error.

The experiments were conducted under the assumption that the illumination of the working area by the built-in LEDs of the multispectral sensors was spatially and angularly uniform. To physically compensate for any possible non-uniformity in the light field and eliminate local optical anomalies, two design and methodological solutions were implemented in the system.

(1) The distance from the sensor matrix to the surface of the material layer (20 mm) and the angle of the LEDs ensured a stable radiation pattern across the entire detection area.

(2) The use of a cylindrical rotating platform with a concentrically offset axis (R=20–25 mm) allowed for continuous adjustment of the position of individual grains within the working zone during a series of measurements. As a result, local micro-zones of increased or decreased illumination were effectively averaged through statistical processing of over 100 discrete measurements.

In developing the methodology, it was assumed that the continuous rotation of the Petri dish completely cancels out the anisotropy of light reflection from individual soybeans through statistical averaging of the signals.

Since individual beans have complex geometric shapes and random spatial orientations (in particular, varying positions of the scar and surface micro-relief relative to the sensor's optical axis), static measurements are subject to high random errors due to local reflections or shadowing. Due to the offset of the cylindrical platform's axis of rotation by a value (R = 20–25 mm), the sensor's detection zone described a circular trajectory on the sample surface. This ensured a continuous change in the set of grains and their microfacets within the sensor's field of view during the experiment.

Statistical averaging of results from over 100 discrete measurements enabled integration of the spectral response from a large number of randomly oriented objects. This completely eliminated the influence of the optical anisotropy of individual grains and enabled us to obtain a reproducible, macroscopically homogeneous spectral "portrait" of the fraction of the material under study.

The fundamental methodology for grain quality assessment and feature extraction used in this study follows the approach described in detail in [19]. This method was adapted for the YOLO11n-seg architecture to enable real-time instance segmentation of soybean fractions.

A test rig was constructed for photographing soybean grain samples (Fig. 4). The photographs were taken in a light-tight chamber under controlled artificial lighting to eliminate the influence of external light.

A 12-megapixel sensor with a fixed focal length was used. Exposure and white balance settings were adjusted manually to ensure consistent color characteristics of the samples.

Images were captured with varying degrees of object coverage in the working area, simulating real-world operating conditions of the separator. A baseline dataset of 100 high-resolution images was prepared.

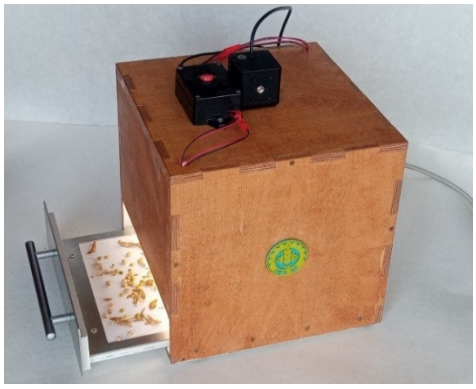

Fig. 4. A test rig for photographing grain samples.

Annotation of masks for instance segmentation was performed in the Roboflow environment. Each object (grain or impurity) was outlined using a polygonal mask to train the YOLO-seg model.

Three object classes were defined according to the sorting tasks: whole grain (Normal Grain), damaged grain (Broken Grain), and organic impurities (MOG).

The data preprocessing process was divided into five sequential stages to evaluate the impact of the sample's quantitative and qualitative characteristics on the accuracy of object segmentation by YOLO11n-seg models (Table 1).

Dataset D1 – Baseline-50. A minimal baseline comprising 50 original images without any additional processing. The goal is to assess the model's ability to generalize on a critically small sample. This stage serves as a baseline for evaluating the effectiveness of all subsequent data augmentation methods.

Dataset D2 – Baseline-100. A quantitative expansion to 100 original images. The goal is to assess the impact of a 200% physical increase in data volume without using software-based augmentation methods. This allows us to isolate the pure effect of scaling the image dataset.

Table 1. Characteristics of datasets for training YOLO11n-seg models.

ID	Dataset type	Number of photos	Key feature	Expected effect
D1	Baseline-50	50	Minimum Sample	Retraining Score
D2	Baseline-100	100	Base Doubling	mAP50 Gain
D3	Geometric	100 (orig) + Aug	Rotate, Flip	Shape Invariance
D4	Optical	100 (orig) + Aug	Brightness/Contrast	Exposure Robustness
D5	Advanced	100 (orig) + Aug	Noise + Blur	Maximum Reliability

Dataset D3 – Geometric invariance. Includes 100 original images and their geometric augmentations: Rotation ±15° (accounting for the random distribution of grains on the platform); Horizontal and vertical flipping; scale 0-10% (simulating seed size variability). The goal is to train the model to recognize objects regardless of their spatial orientation, which is critical for dynamic sorting systems.

Dataset D4 – Optical Robustness. Includes 100 images + optical augmentation: Brightness from -15% to +15%; Contrast ±10%; Saturation ±10%. The goal is to compensate for camera sensor errors caused by changes in brightness across different degrees of

working area coverage. This ensures segmentation stability when the "object/background" area ratio changes.

D5 Dataset – Synthetic Complexity and Robustness. This dataset combines D3 and D4 with advanced augmentation techniques, including Blur (a slight blur to simulate grain micro-movements). The goal is to create the most versatile model capable of operating under conditions of real-world production noise and focus instability.

The YOLO11n-seg model was selected for this study. The YOLO11n-seg models were trained on a specialized NVIDIA Jetson AGX Orin 64GB computing module, which features a 2048-core GPU based on the Ampere architecture and delivers up to 275 trillion operations per second at INT8 precision. The choice of this platform was driven by the need to integrate the developed algorithms into real-time grain-cleaning machine control systems.

The training process was standardized across all five generated dataset types according to the following parameters. The YOLO11n-seg architecture, with decomposition into detection and segmentation heads, ensures a balance between processing speed (real-time) and the accuracy of object mask extraction.

Training continued for up to 300 epochs using an early stopping mechanism with a patience of 50 epochs to prevent overfitting on small datasets. The *AdamW* optimizer was used with an initial learning rate of $\eta = 0.01$ and a batch size of 16. The resolution of the input images was set to 1280×1280 pixels.

Each dataset was randomly split in the following ratio: 80% for training and 20% for validation.

Model validation was performed using two key metrics: the mean average precision for object detection $\mathrm{mAP50}^{box}$ and the mean average precision for segmentation mask construction $\mathrm{mAP50}^{mask}$, which are critical for accurately determining the area of damaged grain and impurities.

3. Results and discussion

3.1. Analysis of reflected signal intensity

Experimental studies provided quantitative measurements of reflected irradiance for the main technological fractions. The measurement results in the visible (VIS) and near-infrared (NIR) ranges are presented in Tables 2 and 3.

Table 2. Average reflected irradiance in the VIS range, $\frac{\mu W}{cm^2}$.

Fraction / Benchmark	450 nm	500 nm	550 nm	570 nm	600 nm	650 nm
Normal grain	8111.9 ± 390.1	1646.3 ± 110.6	4004.0 ± 221.5	4480.5 ± 214.2	863.2 ± 59.6	4791.0 ± 278.2
Broken grain	7182.5 ± 509.1	1225.8 ± 106.2	3406.3 ± 268.6	3955.7 ± 272.4	570.2 ± 51.0	4391.3 ± 404.6
MOG	4994.8 ± 941.9	1012.5 ± 201.6	2329.0 ± 459.5	2697.9 ± 493.1	561.3 ± 116.4	3197.5 ± 525.3
White Standard	19079.5 ± 199.1	4941.3 ± 39.1	10957.6 ± 124.9	10378.6 ± 92.9	3635.5 ± 34.2	8472.2 ± 42.0
Black Standard	3695.4 ± 137.4	238.8 ± 14.4	1817.2 ± 72.1	1158.3 ± 44.3	537.0 ± 29.1	478.0 ± 26.6

Table 3. Average reflected irradiance in the near infrared-range (NIR, 610–860 nm), $\frac{\mu W}{cm^2}$.

Fraction / Benchmark	610 nm	680 nm	730 nm	760 nm	810 nm	860 nm
Normal grain	2430.1 ± 110.9	841.2 ± 60.1	411.3 ± 13.7	244.5 ± 8.5	171.6 ± 6.5	89.5 ± 4.5
Broken grain	2126.5 ± 220.2	692.5 ± 93.6	363.6 ± 23.4	210.9 ± 10.9	146.6 ± 9.8	75.4 ± 6.0
MOG	1432.8 ± 288	569.6 ± 76.3	257.6 ± 43.9	160.4 ± 20.4	112.2 ± 15	59.3 ± 7.3
White Standard	5270.6 ± 48.5	1310.7 ± 7.8	632.1 ± 5.6	353.2 ± 2.5	285.9 ± 2.0	138.3 ± 0.8
Black Standard	1063.9 ± 28.4	91.4 ± 4.7	119.3 ± 2.8	53.5 ± 1.6	44.9 ± 1.4	10.9 ± 0.5

The application of white and black standards enabled the determination of the measurement system's sensitivity limits. It was established that the reflectance of whole soybean grains across all tested spectral channels (spanning from 450 to 860 nm) ranges from 35% to 65% relative to the white standard. This ensures high signal quantization accuracy while avoiding sensor saturation of the AS726x photosensitive matrix. Furthermore, dynamic data acquisition (100 measurements per platform rotation) effectively minimized the impact of random grain orientation. The low standard deviation values, σ, in Tables 2 and 3 confirm that the resulting spectral signatures are stable characteristics of the fraction rather than stochastic, isolated measurements.

Analysis of the tables shows that normal grain has the highest reflected irradiance across all spectral channels (450–860 nm), whereas impurities (MOG) consistently exhibit lower values. For example, at 450 nm, the reflected intensity of impurities ($4994.8 \pm 941.9\,\mu W/cm^2$) is nearly half that of soybean grains ($8111.9 \pm 390.1\,\mu W/cm^2$). Low standard deviation values confirm the effectiveness of the proposed averaging algorithm during sample rotation.

Analysis of the obtained data confirms the metrological reliability of the developed experimental setup. The reflected irradiance of normal grain across all VIS-range channels falls within 35% to 65% of the white reference values, ensuring a high signal-to-noise ratio without the risk of sensor saturation.

Low standard deviation values for the normal grain samples indicate the correctness of the dynamic data acquisition algorithm during the rotation of the Petri dish. This allows the elimination of the influence of individual grains' shape and orientation in the layer. Furthermore, the coefficient of variation (CV) for normal grain is remarkably low, remaining within the 5–7% range across the key spectral channels, which confirms the uniform optical properties of the seed coat.

In MOG, the *CV* reaches 20%. The high coefficient of variation for impurities (MOG) is due to their heterogeneous physical structure and varying chemical composition, which creates specific noise in the spectral response that is easily identified by neural network algorithms.

The data in Tables 2 and 3 demonstrate specific spectral behaviors: the reflected irradiance exhibits a multi-peak non-linear profile in the VIS range and a monotonic attenuation as the wavelength increases across the NIR spectrum.

At 610 nm, the difference in reflected irradiance between normal (~2430 μW/cm²) and broken (~2120 μW/cm²) grains is about 12–14%. This indicates that damage to the soybean hull alters its diffuse reflectance even in the NIR range. At the same time, MOG (~1400 μW/cm²) is almost half that of normal grain. This is an ideal metric for automatic segmentation and a strong case for using a YOLO11n-seg-type neural network. The model can rely not only on shape but also on pixel intensity.

3.2. Analysis of spectral reflectance curves

To obtain objective characteristics independent of the brightness of the sensor's LEDs, the intensity was converted into reflectance coefficient R_{abs}. Absolute values of the reflectance coefficients were calculated based on the data in Tables 2 and 3 and are presented in Figs. 5 and 6.

As seen in the graphs, the largest spectral distance between the fractions occurs at 450 nm and 650 nm. At the 650 nm channel, whole grain exhibits $R_{abs} \approx 44.1\%$, while for MOG, this value does not exceed 28.4%. Such pronounced contrast serves as a physical prerequisite for successful object recognition by the neural network.

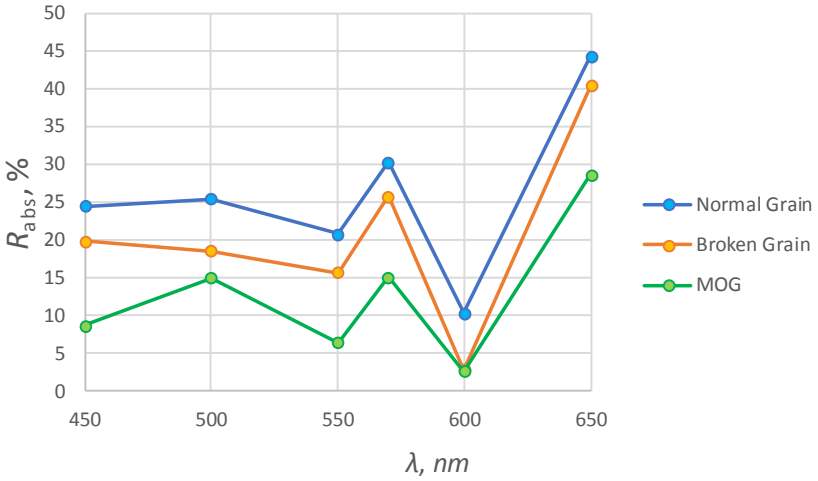

Fig. 5. Spectral dependencies of the reflectance coefficient R_{abs} in the visible range.

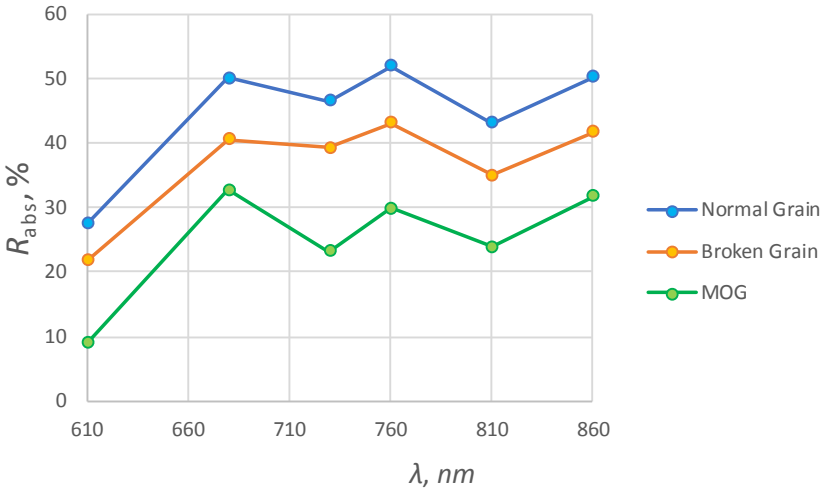

Fig. 6. Spectral dependencies of the reflectance coefficient R_{abs} in the near-infrared range.

The reflectance graph (Fig. 5) shows a sharp drop in the reflectance coefficient R_{abs} for all samples at 600 nm. For whole soybean seeds, reflectance drops to approximately 10%. For impurities (MOG) and broken grain, reflectance falls nearly to the level of the black standard. This indicates the presence of a specific endosperm pigment or structural absorption characteristic of MOG in this range. Dry pod shells (lignified tissue) absorb light in this zone, resulting in minimal reflectance. Since the spectral divergence in R_{abs} values between soybeans and MOG is highest at 600 nm (with soybean grains exhibiting a five-fold higher reflectance than impurities), this channel serves as an effective marker for generating binary masks in preprocessing algorithms.

In the 600–650 nm region, a rapid increase in the absolute reflectance coefficient, R_{abs}, known as the "red edge" effect, is characteristic of plant tissues. The difference between the reflectance curves of normal and broken grains (R_{abs} ~25% versus 20% at 450–500 nm) likely reflects individual variability in the pigmentation of soybean seed coats. The local reflectance maximum at 500 nm and the rise at 650 nm are clear indicators of chlorophyll remaining in immature pods and, to some extent, in immature whole seeds. Chlorophyll exhibits a "green peak" of reflectance near 550 nm and a sharp increase starting at 650 nm ("red edge").Consequently, the MOG class can be described as "spectrally heterogeneous." While the presence of chlorophyll in immature elements creates variability in the visible range (450–650 nm), the 600 nm dip remains a stable feature for most organic impurities.

Fig. 6 shows a characteristic zone at 610 nm (the onset of the "red edge"). Reflectance here is lowest across all samples, consistent with the visible-range reflectance data (Fig. 5). The near-infrared (NIR) reflectance spectrum features characteristic peaks at 680 nm and 760 nm. For whole and broken soybean grain (blue and orange lines), reflectance reaches 40–50%, whereas for impurities (green line), it remains within the 25–30% range.

A stable difference of 15–20% in R_{abs} values between grain and impurities in the NIR range is a significant advantage. In the visible light spectrum (RGB), dry pods and yellow soybeans may appear similar in brightness; however, their reflectance profiles diverge markedly in the NIR spectrum, enabling unerring identification of MOG. The observed decreases in structural reflectance at 730 nm and 810 nm correspond to the macro-structural and morphological attenuation characteristics of the tested biological materials rather than to localized chemical absorption. In this multi-spectral setup, these variations are used primarily as robust geometric and amplitude classification features for the YOLO11n-seg model, thereby bypassing the need for complex, computationally expensive chemometric modeling.

The use of NIR spectroscopy in the 610–860 nm range enabled the identification of stable spectral markers at 680 nm and 760 nm. It was established that the relative reflectance coefficient R_{abs} for whole soybean seeds at these points exceeds that of organic impurities by 15–22%. This ensures high reliability for the YOLO11n-seg segmentation algorithm when identifying objects with similar visual characteristics in the visible spectrum.

3.3. Model training and analysis of results

To evaluate the developed approaches, a summary performance matrix for the neural network was generated (Table 4), illustrating the evolution of quality metrics as the system transitioned from baseline detection conditions to high-resolution hybrid models.

Experimental results on the D1 dataset demonstrated the high performance of the chosen architecture. After 300 training epochs, the model achieved an average segmentation accuracy (mAP50, mask) of 0.956.

Table 4. Comparative performance analysis of soybean instance segmentation models across various dataset formation strategies and spatial resolutions.

ID	Dataset	Resolution	Mask mAP50	Mask mAP50–95	BG Mask mAP50–95	Inference, ms (FPS)
D1	Baseline-50	640×640	0.956	0.785	0.822	18.6 (~54)
D2	Baseline-100	640×640	0.94	0.775	0.788	17.3 (~58)
D3	Geometric	640×640	0.946	0.794	0.789	16.2 (~62)
D4	Optical	640×640	0.948	0.772	0.772	16.1 (~62)
$D5_{640}$	Hybrid Robustness	640×640	0.952	0.791	0.784	16.3 (~61)
$D5_{1280}$	Advanced High-Res	1280×1280	0.956	0.872	0.885	60.3 (~17)

A detailed analysis of the results by target class (Fig. 7) shows that the highest contour segmentation accuracy is achieved for normal soybean grains (class NG), with a mean accuracy of mAP50=0.989. High recognition performance was also observed for damaged grains (class BG), for which mAP50=0.980.

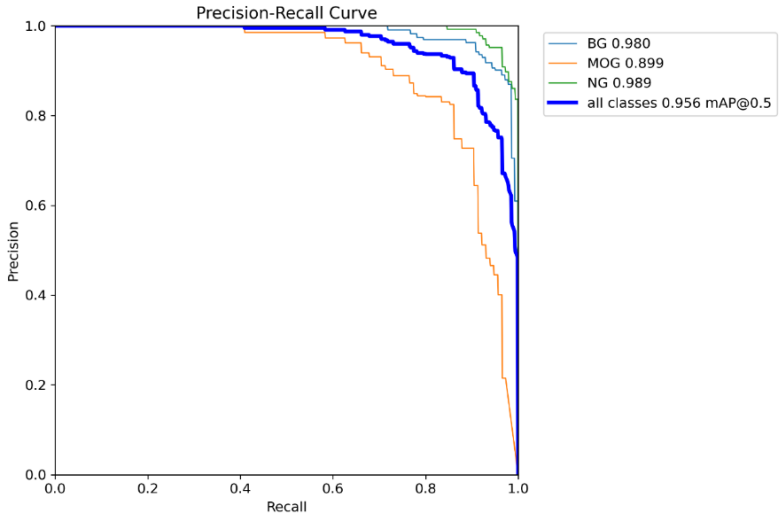

Fig. 7. Precision-Recall curves for the example segmentation of object masks for the base dataset D1: NG – standard soybean grains; BG – broken/damaged grains; MOG – organic impurities; all classes – the model's integral average accuracy.

The slightly lower value for the organic impurities class (MOG: mAP50=0.899) is explained by the high variability of the morphological features of plant residues (stems, pod fragments, leaves) compared to the relatively homogeneous geometric shape of soybean seeds. The integral value of the model's mean accuracy across all classes is mAP50=0.956, confirming the high precision of the proposed rapid analysis method.

The inference speed on the NVIDIA Jetson AGX Orin platform was 18.6 ms per image, enabling real-time sorting. The stability of the training is confirmed by low loss values (*Box loss*: 0.35; *Seg loss*: 0.45), indicating no overfitting.

When the sample size was increased to 100 images (dataset D2), the Early Stopping algorithm was applied with a patience of 50. The best segmentation results were recorded at the 140th epoch (Fig. 8), after which the accuracy metrics plateaued on the validation set.

The final mAP50 metric for masks was 0.94. It is important to note the increase in segmentation accuracy for organic impurities (MOG) to 0.913, which indicates an improvement in the model's ability to extract features of objects with low reflectivity (according to the spectral data in Fig. 5). The slight decrease in the overall mAP compared to D1 is explained by the increased complexity and variability of the expanded test set (731 instances versus 400), which makes the obtained data more representative of industrial conditions.

The implementation of geometric augmentations (D3 dataset) enabled us to achieve the highest recall rate ($Recall$=0.961) for the Broken Grain class. This is critical for minimizing impurities in the final product. The improvement of the $mAP50-95$ metric to 0.794 indicates high accuracy in approximating object contours, which is a necessary condition for the precise operation of the separator's actuators.

A set of optical enhancements was applied to improve the robustness of segmentation algorithms against photometric noise. In particular, an *Exposure* variation of ±10% allowed for compensation of the system's reflectance nonlinearity at different seed flow densities, as confirmed by spectral data (Fig. 5). *Hue* and *Saturation* augmentations were implemented to simulate varying moisture content in the grain mixture.

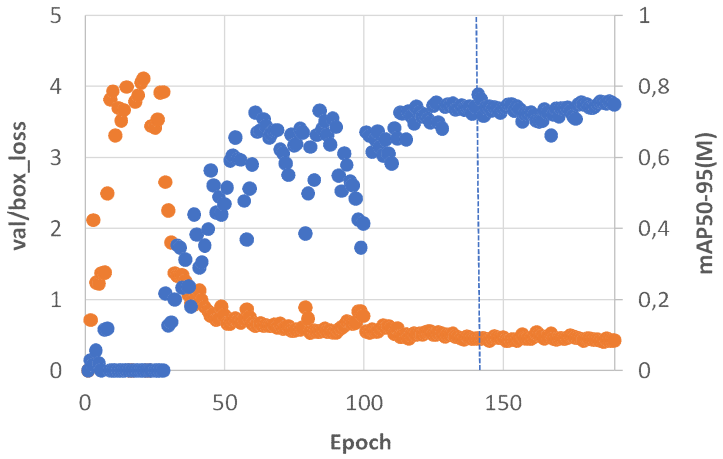

Fig. 8. Combined dynamics of the object localization loss function (val/box_loss , orange markers) and the integral mask segmentation accuracy metric (mAP50-95(M) , blue markers) for dataset D2.

An analysis of the training results on the D4 dataset (Optical Augmentation) demonstrated the model's highest overall performance in object recognition under varying environmental lighting conditions, with an mAP50 of 0.948. At the same time, artificially varying the Exposure by ±10% and the Brightness by ±15% led to a redistribution of accuracy across classes. Changing the optical profile improved segmentation for the Broken Grain class but caused a slight decrease in the mAP50-95 metric for the MOG class (to 0.708). This is due to the physical nature of the objects: the low absolute reflectance of organic impurities in the visible spectrum, combined with additional frame darkening, shifts the operating points of the pixels into the camera sensor's digital noise region, which complicates precise tracing of polygonal mask boundaries.

To obtain the final convolutional model (D5 dataset), a comprehensive combined augmentation method was developed. The goal of this stage was to simultaneously model

both the spatial-geometric factors of the seeds' chaotic motion and the dynamic photometric disturbances directly within the separator's working area.

Particular attention was paid to the integration of the *Blur* function (up to 1.5 px) when creating D5. Under real-world operating conditions of the separator, the screen operates at specific frequencies and amplitudes, causing micro-instability of the camera's optical axis and dynamic "blurring" of object contours (motion blur) as seeds move while falling or sliding. The implementation of controlled edge blurring, combined with variations in brightness and geometric rotations, allows the YOLO11n-seg model decoder to be artificially trained to reconstruct mask topologies even under conditions of partial loss of focus.

The integration of spatial-geometric and optical-dynamic augmentation methods into the D5 combined dataset ensured the highest robustness of the YOLO11n-seg model under the separator's operational conditions. The implementation of controlled digital edge blurring (Blur up to 1.5 px) allowed us to simulate the dynamic image blurring caused by tray vibration. Unlike the isolated use of photometric transformations (dataset D4), an adapted brightness and exposure adjustment step of ±10%, combined with spatial rotation, increased the accuracy of mask segmentation to mAP50=0.952 and mitigated the decline in metrics for the MOG (mAP50-95 = 0.745). The resulting model exhibits a high capacity for feature generalization, ensuring stable real-time soybean seed quality analysis (inference speed on the NVIDIA Jetson AGX Orin platform is 16.3 ms/frame).

To study the effect of spatial resolution on the accuracy of identifying microdefects in seeds (cracks, chips), the input tensor was upscaled to 1280×1280 pixels. Experimental training of the combined D5 dataset with a batch size of B=16 was performed directly on the NVIDIA Jetson AGX Orin edge computer (64 GB). Due to the unified memory architecture, peak VRAM consumption stabilized at 22.5 GB, eliminating the risk of overflow errors and ensuring the correct functioning of the batch normalization layers. The average computation time per epoch was 1 minute 15 seconds, confirming the high computational efficiency of Jetson mobile platforms for real-time inference with high-precision YOLO11n-seg segmentation models.

To visually assess the effectiveness of sorting fraction recognition, a comparison is shown between the true label matrices (Fig. 9a) and the model's predictions (Fig. 9b) on a random validation sample.

Visual analysis confirms the neural network's high capability for instance segmentation, even under high-density and overlapping conditions within the frame. The model accurately differentiates geometrically homogeneous areas of conditioned grain (class NG, with a confidence level up to *Conf* = 1.0) and localizes areas of tissue destruction and chips on damaged seeds (class BG, with the vast majority of values *Conf* ≥ 0.9). Plant residues and complex-shaped impurities (MOG class) are reliably outlined with an average confidence level of 0.8–0.9, which completely eliminates the risk of their erroneous passage into the good grain fraction.

Prospects for further research lie primarily in the software and hardware optimization of neural network inference, where transitioning from the standard PyTorch environment to deep model optimization via NVIDIA TensorRT and INT8 weight quantization could potentially double the frame rate (FPS) on the Jetson Orin platform with minimal impact on segmentation precision. Furthermore, scaling the system involves moving from 6-channel

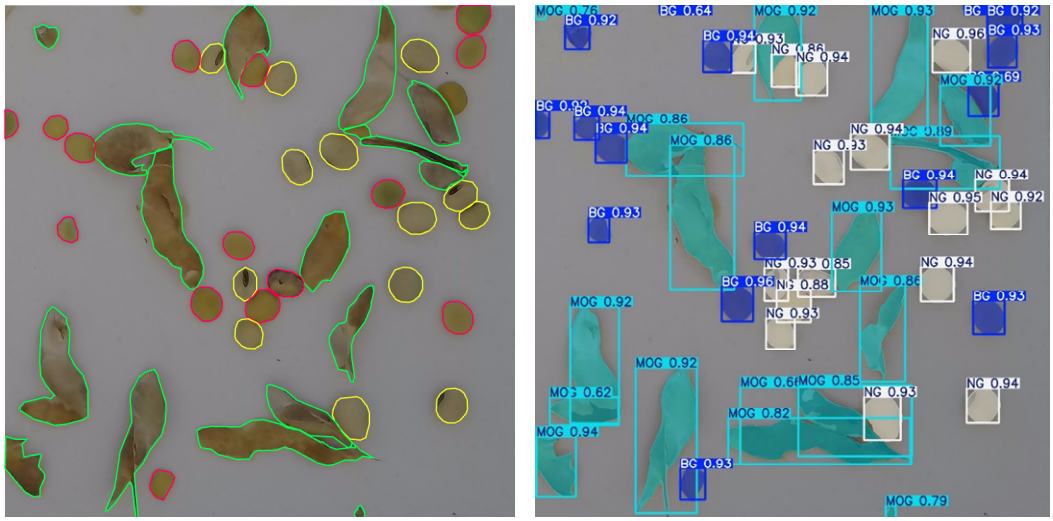

a) b)

Fig. 9. Visual comparison of instance segmentation results for soybean fractions on a validation image mosaic: a) original expert annotation of the dataset for normal grain (NG, yellow), damaged grain (BG, pink), and MOG (green); b) masks and classes generated by the YOLO11n-seg model, including confidence scores.

discrete analysis to integrating full-fledged multispectral cameras directly into the YOLO11n-seg processing pipeline, thereby enabling real-time classification based on the unique "spectral fingerprint" of each pixel rather than RGB geometry alone. Additionally, given that seed moisture significantly shifts absorption features in the NIR range, further experiments will evaluate grain at various drying stages to establish adaptive segmentation thresholds for energy-efficient post-harvest processing. Ultimately, the developed architecture will be tested using transfer learning to validate its adaptability to other agriculturally critical crops–such as corn, wheat, and rapeseed–with the goal of creating a universal, high-throughput intelligent quality control module for smart farming applications.

4. Conclusion

This paper presents a comprehensive approach to identifying the fractional composition of soybean seeds, based on the synergy of multichannel spectral analysis and neural network architectures for instance segmentation.

It was established that the most representative "contrast window" for separating soybean seeds from organic impurities (MOG class) is the 610–680 nm range, where the largest absolute gap in reflectance coefficients is observed. Despite the spectral heterogeneity of impurities in the visible spectrum due to chlorophyll, the intensity dip at 600 nm remains a stable identifying feature for most types of plant residues.

The analysis of 300 spectral readings and the use of a dynamic data-collection method helped minimize the effects of random grain orientation. The low standard deviation ($\sigma < 5\%$) in the NIR range confirms the method's high reproducibility and the stability of soybean spectral characteristics, providing a basis for training a neural network.

It was revealed that the absolute reflectance coefficient of the soybean endosperm in the blue (450 nm) and green (500 nm) spectral channels is 15–20% higher than that of an intact seed coat. Integrating this spectral feature, along with geometric analysis (eccentricity and mask area), into the YOLO11n-seg model achieved an overall classification accuracy of mAP50 = 95.6%.

Increasing the input tensor resolution to 1280 pixels proved critical for micro-defect identification. This improved the strict segmentation metric mAP50-95 to 0.872, yielding a 10.1% increase in precision for the broken grain class compared to the standard 640-pixel configuration.

Experimental deployment on the NVIDIA Jetson AGX Orin edge platform demonstrated real-time data processing capability at approximately 17 FPS with a measured inference latency of 60.3 ms. The combination of spectral precision and high spatial resolution of YOLO11n-seg justifies recommending the developed system for integration into intelligent optical separators and automated systems for laboratory grain quality control.

Funding. This study was conducted as part of Project No. 2025.02/0002, funded by the National Research Foundation of Ukraine for scientific research and development.

Conflicts of interest. The authors declare no conflicts of interest. The authors declare that they have no known competing financial interests or personal relationships that could have appeared to influence the work reported in this paper.

Author Contributions. Conceptualization, S.S.; methodology, S.S.; software, S.S. and A.K.; validation, S.S.; formal analysis, S.S.; investigation, S.S. and A.K.; resources, S.S.; data curation, S.S.; writing–original draft preparation, S.S.; writing–review and editing, S.S.; visualization, S.S.; supervision, S.S.; project administration, S.S. All authors have read and agreed to the published version of the manuscript.

References

1. Sunil, C. K., Ashish, R., Chidanand, V., & Shobika, S. (Eds.) (2025). *Emerging Non-destructive Technologies for Food Quality Analysis*. Cham. Springer.
2. Chung, S. O., Choi, M. C., Lee, K. H., Kim, Y. J., Hong, S. J., & Li, M. (2016). Sensing Technologies for Grain Crop Yield Monitoring Systems: A Review. *Journal of Biosystems Engineering*, *41*, 408-417.
3. He, W., Jingtao, H., Lei, G., & Yanfeng, J. (2016). Development and optimization of a novel grain flow sensor based on PVDF piezoelectric film. International Journal of Agricultural and Biological Engineering, 9(4), 141–150.
4. Afandi, A., Khasani, D., Catrawedarma, I., & Wijayanta, S. (2024). The development of the ultrasonic flowmeter sensors for mass flow rate measurement: A comprehensive review. *Flow Measurement and Instrumentation*, *97*, 102614.
5. Flor, O., Palacios, H., Suárez, F., Salazar, K., Reyes, L., González, M., & Jiménez, K. (2022) New Sensing Technologies for Grain Moisture. *Agriculture*, *12*(3), 386. doi: 10.3390/agriculture12030386
6. Ni, X. D., Li, M. L., Li, F. L., Dai, Z.X., Xing, C. X., Wang, F., …He, Z. Z. (2026). Magnetoelastomer-based grain flow sensor for combine harvesters. *Computers and Electronics in Agriculture*, *244*, 111447.
7. Musse, M., Gimbert, I., Diascorn, Y., Quellec, S., Challois, S., Faulds, C.B., & Lucas, T. (2026). Surplus bread fermentation by Pleurotus ostreatus monitored by magnetic resonance imaging. *Journal of Food Engineering*, *412*, 112967.
8. Cardoso Jesus, J.L., Bilhalva, N.D., Santana, D.C., Teodoro, L.P., Teodoro, P.E., & Coradi, P.C. (2026). Classification of the Physicochemical Quality of White, Parboiled, Black and Red Rice in Storage and Processing Units Integrating Near-infrared Spectroscopy, Hyperspectral Sensing, and Machine Learning Models. *Journal of Biosystems Engineering*, *51* (1), 8.
9. Pancorbo, J.L., Alonso-Ayuso, M., Camino, C., Raya-Sereno, M.D., Zarco-Tejada, P.J., Molina, I., …Quemada, M. (2023). Airborne hyperspectral and Sentinel imagery to quantify winter wheat traits through ensemble modeling approaches. *Precision Agriculture*, *24* (4), 1288–1311.
10. Lazzoni, V., Brizi, D., Staglianò, N., Giordano, C., Pecoraro, E., Anichini, M., …Rossi, R. (2024). Development of a microwave sensor for the non-invasive detection of plant responses to water stress: A practical application on maize (Zea mays L.). *Biosystems Engineering*, *246*, 191–203.
11. Runtao, L., Xianliang, W., Yanchun, Y., Zhongcai, W., Hua, Z., & Xiangcai, Z. (2022). Research on intelligent detection technology of seed planter. *Journal of Chinese Agricultural Mechanization*, *43* (5), 93–101.
12. Yue X., Tan X., Xiao J., Chen J., Ouyang H., & Lan Y. (2026). Research status and development trend of intelligent detection technology for rice pest. *Journal of South China Agricultural University*, *47* (2), 196–208.
13. Yang, Z.-K., Li, P.-F., Ding, L.-L., He, C.-Z., & Zhang, K.-P. (2026). Baling process of a belt-type baler based on a discrete element-multi-body dynamics coupling method. *Smart Agricultural Technology*, *14*, 102021.

14. Oeser, L., Wessely, B., Samala, N., Hillemann, L., Göhler, D., Müller, J., …Lienig, J. (2025). Statistical signal analysis for optical aerosol spectrometers: Closing the gap between single particle counting and signal fluctuation analysis. *Journal of Aerosol Science*, *188*, 106611.
15. Ahuome, B. A., Ahmad, I., & Isah, R. H. (2025). The use of MEMS accelerometer in vibration monitoring of white sugar variant centrifugal machine at Dangote sugar refinery NUMAN. *Journal of Basics and Applied Sciences Research*, *1*(1), 184–191.
16. Mendoza, P.T.D., Armstrong, P.R., & Siliveru, K. (2025). Hyperspectral Imaging. In: Sunil, C.K., Rawson, A., Chidanand, D.V., Shanmugasundaram, S. (eds) Emerging Non-destructive Technologies for Food Quality Analysis. Springer, Cham.
17. Guo, T., Zhang, T., Lim, E., Lopez-Benitez, M., Ma, F., & Yu, L. (2022). A Review of Wavelet Analysis and Its Applications: Challenges and Opportunities. *IEEE Access, 10*, 58869 - 58903.
18. Chen, Z., Wu, W., Dou, J., Liu, Z., Chen, K., & Xu, Y. (2021). Design and Analysis of a Radio-Frequency Moisture Sensor for Grain Based on the Difference Method. *Micromachines*, *12*(6), 708.
19. Stepanenko S., Kuzmych A., Kharchenko S., Borys A., Dnes V., Volyk D., & Kalinichenko R. (2025). A machine vision approach for grain quality control during separation. *Journal of Engineering Sciences (Ukraine)*, *12*(1), E9–E17.

Stepanenko, S., Kuzmych, A. (2026). Intelligent Soybean Seed Fraction Segmentation System Based on the Integration of Spectral Signatures and Precision Neural Network Architectures. *Ukrainian Journal of Physical Optics*, *27*(4), 04016 – 0433.
doi: 0.3116/16091833/Ukr.J.Phys.Opt.2026.04016

Анотація. *У цьому дослідженні представлено інтелектуальну систему контролю якості насіння сої, яка інтегрує багатоканальний спектральний аналіз із сегментацією екземплярів на базі нейромережі YOLO11n-seg. Визначено спектральне «контрастне вікно» в діапазоні 610–680 нм для оптимального відокремлення домішок, а також зафіксовано підвищення абсолютного коефіцієнта відбивання на 15–20% у спектральних каналах 450 нм і 500 нм для пошкодженого насіння. Для покращення детекції мікродефектів було використано гібридний набір даних, що імітує динамічне розмиття кадру. Збільшення вхідної роздільної здатності зображення до 1280 пікселів істотно покращило чіткість визначення меж об'єктів, забезпечивши підвищення точності ідентифікації битого зерна на 10,1% порівняно зі стандартними моделями з роздільною здатністю 640 пікселів. Апаратна реалізація на межовій платформі NVIDIA Jetson AGX Orin забезпечила швидкість обробки даних у реальному часі на рівні 17 FPS із загальною точністю класифікації 0,956. Отримані результати формують фізичний та алгоритмічний базис для високоточного автоматизованого сортування насіння в інтелектуальних сільськогосподарських застосуваннях.*

Ключові слова: *спектроскопія дифузного відбивання, мультиспектральна візуалізація, межові обчислення штучного інтелекту, оптичне сортування, коефіцієнти відбивання, спектральна сигнатура.*